Defect evolution under intense electronic energy deposition in uranium dioxide

G Gutierrez, H Guessous, D Gosset, M Bricout, I Monnet, F Garrido, C Onofri, G Adroit, A Debelle

Defect evolution under intense electronic energy deposition in uranium dioxide

G. Gutierrez[1], H. Guessous[1], D. Gosset[2], M. Bricout[1], I. Monnet[3], F. Garrido[4], C. Onofri[5], G. Adroit[1], A. Debelle[4]

[1] Université Paris-Saclay, CEA, Service de Recherches de Métallurgie Physique, 91191, Gif-sur-Yvette, France.

[2] Université Paris-Saclay, CEA, Service de Recherches de Métallurgie Appliquée, 91191, Gif-sur-Yvette, France.

[3] Centre de recherche sur les ions, les matériaux et la photonique, Normandie Université, ENSICAEN, UNICAEN, CEA, CNRS, CIMAP, 14000 Caen, France.

[4] Laboratoire de Physique des 2 infinis Irène Joliot-Curie (IJCLab), Université Paris-Saclay, Orsay, France.

[5] CEA, DES, IRESNE, DEC, Cadarache, F-13108 St Paul lez Durance, France.

Abstract

The coupled effects of nuclear and electronic energy losses were investigated in uranium dioxide (UO_2). Single and sequential ion irradiations were carried out with 92 MeV Xe ions and 0.9 MeV I ions. Raman spectroscopy and X-ray diffraction analyses were combined with the inelastic thermal spike (iTS) model to investigate the effect of electronic ionizations on the ballistic damage. It appears that the high-energy ions induce a significant change in the defect distribution with an amplitude that depends on the level of pre-existing disorder. This change essentially consists in an acceleration of the dislocation loops into dislocation lines, a process that is accompanied by a stress relaxation. Surprisingly, with the fluence increase of 92 MeV Xe ions, the stress starts to increase again, highlighting a possible synergetic effect between the pre-existing defects and those generated by the 92 MeV Xe ions irradiation.

Keywords: UO_2, *Swift heavy ions, Ion irradiation, Raman, XRD, Nuclear ceramic*

*Corresponding author

E-mail: gaelle.gutierrez@cea.fr

INTRODUCTION

Fluorite-type oxides such as CeO_2, ZrO_2 and UO_2 crystalline compounds are very radiation resistant. Indeed, even after ion irradiations at high doses, no amorphisation was observed in these materials [1-3]. This is one of the reasons why UO_2 is the main compound of the nuclear fuel worldwide. During the in-reactor operations, the fission chain reaction induces the formation of fission fragments (FF) with a kinetic energy ranging from 70 to 100 MeV, corresponding to a maximum electronic stopping power (S_e) of around 22 keV.nm^{-1}. The FF lose firstly their energy by inelastic collisions with the target electrons inducing electronic ionizations and excitations. Studies of high-energy ion irradiations in UO_2 have revealed a track formation process along the ion path for an electronic stopping power above 20 keV.nm^{-1} [3, 4]. These tracks are the signature of complex defect formation phenomena materialized by microstructural distortions and deformations [5-7] and atomic displacements [8]. During the FF slowing down, the electronic energy loss decreases while the nuclear counterpart (S_n) increases, leading to atomic displacements via simple (ballistic) collision cascades, a process much more investigated and understood. Studies of low-energy ion irradiations in UO_2 revealed the formation of dislocations [9-12] and small vacancy clusters [13, 14]. Interestingly, the microstructure after low- or high-energy ion irradiation appears to be very similar in UO_2 (and ZrO_2 as well), despite the completely different energy transfer processes involved in the two cases.

If the separate effects on the microstructure of S_e and S_n type irradiations in UO_2 are relatively well established, coupled effects received much less attention and are hence only weakly documented. The coupling between the nuclear and electronic energy (below 12 keV.nm^{-1}) losses has yet been shown to have a significant impact on the defect evolution [15-17]. Depending on the deposited electronic energy level, the defect mobility seems to be more or less activated, affecting the disordering rate process and inducing an acceleration of the dislocation evolution kinetics [18]. This work seeks to address the influence of a higher (*i.e.*, > 12 keV.nm^{-1}) electronic energy loss level. For this purpose, pre-irradiated UO_2 samples with low-energy ions were exposed to 92 MeV Xe ions having a S_e of 23 keV.nm^{-1}. The separated effects of each ion (low- and high-energy) was firstly investigated. The influence of electronic excitations was then determined by performing a sequential irradiation. The experimental results obtained by using Raman spectroscopy and X-ray diffraction (XRD) were combined with simulations using the inelastic thermal spike (iTS) model.

EXPERIMENTAL METHODS

Sample preparation

UO_2 polycrystalline pellets with a density of 98% of the theoretical one (i.e. 10.952 g.cm^{-3}) were cut to discs (thickness: 500 µm) and polished on one side. To remove the damage induced by polishing and maintain their stoichiometry (O/U = 2.00), several steps were successively carried out. The discs were first annealing at 1973 K for 24 h under an Ar-H_2 (5%) atmosphere, then mirror-polished with colloidal silica suspension and annealed under the same Ar-H_2 (5%) atmosphere at 1673 K for 4 h. The average grain size of polycrystalline UO_2 pellets was estimated at 7.6 µm. The lattice parameter of those crystals

is 0.5473 ± 0.0002 nm, in agreement with the commonly admitted value for stoichiometric UO_2 (0.5471 nm) [19, 20].

Irradiation experiments

To study the effect of ballistic damage, irradiations at low-energy with 0.9 MeV I (S_n) ions are performed at the JANNuS-Saclay facility at ion fluences of 10^{14} and 10^{15} cm^{-2} using the JAPET accelerator [21]. In order to determine the influence of electronic excitations, irradiations at high-energy with 92 MeV Xe (S_e) ions were carried out on the GANIL platform on the IRRSUD beamline. The irradiation sequences are summarized in table 1.

Sample denomination	Irradiation sequence	Fluence (cm^{-2})
S_n	Single-beam: 900 keV I	10^{13} - 10^{14} - 10^{15}
S_e	Single-beam: 92 MeV Xe	10^{13} - 10^{14}
S_n+S_e	Sequential irradiation: 0.9 MeV I and 92 MeV Xe	10^{14} (900 keV I) and 10^{13} or 10^{14} (92 MeV Xe)
S_n+S_e	Sequential irradiation: 0.9 MeV I and 92 MeV Xe	10^{15} (900 keV I) and 10^{13} or 10^{14} (92 MeV Xe)

Table 1: Ion irradiation parameters for single (S_n or S_e) and sequential (S_n+S_e) ion irradiation conditions: the irradiation sequences and the corresponding high- (S_e) and low-energy (S_n) ion fluences.

The separated effect of ballistic and electronic energy losses were studied by single ion beam irradiation with low (S_n) or high (S_e) energy ion irradiation. The influence of electronic energy loss on ballistic damage was investigated by performing high energy irradiation on pre-damaged sample at low energy. Different ion fluences were used.

Figure 1 presents simulations performed with the BCA code Iradina using the full-damage cascade mode for the 0.9 MeV I and 92 MeV Xe ions [22]. The threshold displacement energies of 40 and 20 eV were used for U and O, respectively. The 0.9 MeV I ions (S_n) are implanted on the first micrometer (< 0.5 µm) and generated a maximum of 0.7 dpa for a fluence of 10^{14} cm^{-2}. In the first micrometer corresponding to the region affected by the two beams (S_n and S_e), the S_e irradiation induces mostly electronic ionizations. Regarding the high energy ion (S_e), the energy loss is mainly electronic over the first micron reaching 23 $keV.nm^{-1}$ at the surface. The maximum displacement per atoms (dpa) on 1 µm for an ion fluence of 10^{14} cm^{-2} is 0.04 dpa for the S_e ions.

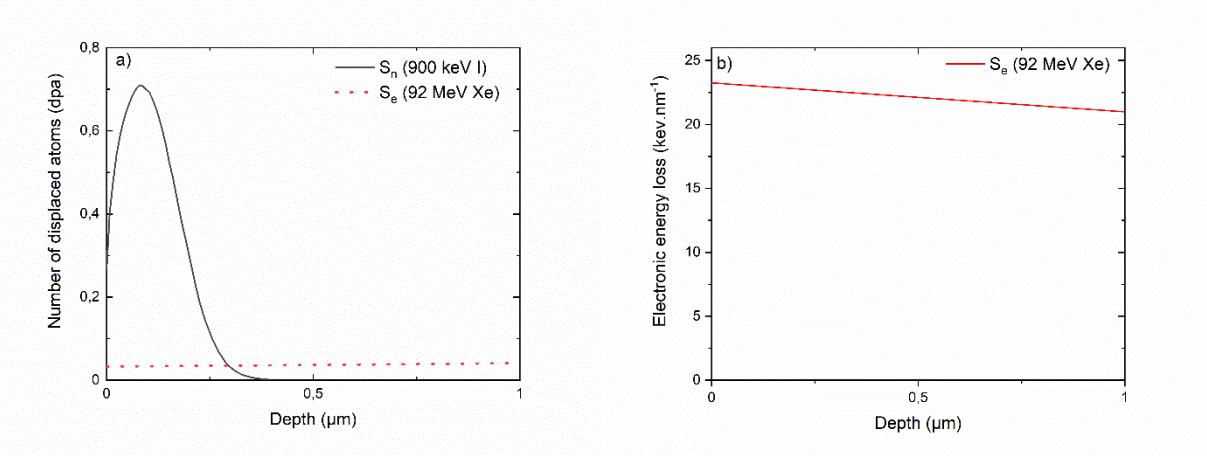

Figure 1: (a) Damage ion profiles for a fluence of 10^{14} cm^{-2} vs depth for UO_2 irradiated with 0.9 MeV I (S_n regime) and 92 MeV Xe (S_e regime) ions and (b) electronic energy loss vs depth for UO_2 irradiated with 92 MeV Xe (S_e regime) ions. Calculations were performed using the Iradina code.

Characterization methodology

Raman analyses using an Invia Reflex Renishaw spectrometer coupled with a Leica microscope (x 100) with a frequency-doubled Nd:YAG (532 nm) laser and a 2400 groove / mm grating were carried. A laser power less than 1 mW was used to avoid the UO_2 oxidation. The Raman spectrometer was calibrated with a silicon single crystal. Raman mapping of the samples surface were performed for 30 grains to determine an average spectrum independent of the grain orientation. The fitting module of the WiRE Raman Spectroscopy software (Renishaw) was used for the spectra simulation assuming Voigt profiles. The accuracy on band position deduced from the spectrum simulation is estimated at ± 0.5 cm^{-1}.

XRD measurements were performed with an INEL set-up that includes a Ge(111) monochromator to select only the $CuK_{\alpha 1}$ radiation, and a fixed 120° 2θ-range curved position sensitive detector (PSD). The incidence angle of the X-rays was set at an angle ω=*2 °,* and 2θ-scans were hence recorded over the entire angular range covered by the PSD. Note that this incidence angle corresponds to an X-ray probed depth of ~280 nm considering an attenuation factor of 90 % [23]. The spinning mode was used to limit texture effects and to increase the statistics that is limited by the large grain size. In order to determine the strain/stress state of the irradiated crystals, we used the $\sin^2\Psi$ method described in details in [24, 25]. The exact method and procedure used in the current work are described in our previous study [17]. Note yet that, as we performed 2θ-scans, we implemented the multiple *hkl* reflections method so that the angle Ψ varied with the Bragg angle of the probed reflections: $\Psi = \theta_{Bragg}^{hkl} - \omega$ [26]; an advantage of this approach is to keep constant the X-ray penetration depth.

It is important to mention that these two techniques, owing to the physical phenomena they rely on, provide somehow different and complementary information on the irradiation effects. First, the probed thickness for XRD is here limited to less than 300 nm, which corresponds only to the Iradina-predicted damage region. In contrast, with Raman, a 1-µm thickness is analyzed in our analysis conditions [36], which includes both a pristine region for the sole S_n irradiation and part of the sole S_e-affected region for

the corresponding irradiation. Second, as we are monitoring the strain and stress levels with XRD, we are sensitive to long-range effects, i.e., to the presence of defects (and hence, disorder) that lead to correlated atomic displacements; in other words, the local disorder such as that studied by following the XRD peak width is not considered here. In contrast, the Raman signal is more sensitive to the local disorder which is affecting both the intensity and the width of the T_{2g} and LO bands (note that the T_{2g} peak shift is related to long-range effects and can provide information on the lattice strain).

RESULTS

Decorrelated effect of nuclear and electronic energy losses

The local disorder induced either by the S_n or S_e ions as function of the ion fluence was investigated by Raman spectroscopy (Fig. 2).

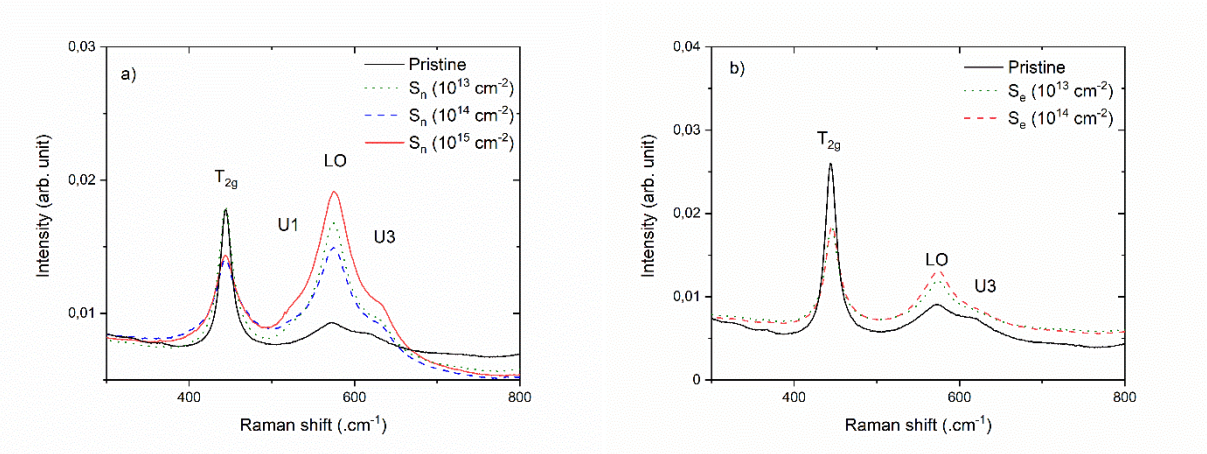

Figure 2: Raman spectra of a UO_2 irradiated with 0.9 MeV I (S_n) ions at fluences of 10^{13}, 10^{14} and 10^{15} cm^{-2} and with 92 MeV Xe (S_e) ions at an ion fluence of 10^{13} and 10^{14} cm^{-2}. The considered Raman spectra correspond to the average spectra measured in a Raman map of 30 grains.

For the pristine sample, one band with a high intensity is exhibited at 446 cm^{-1} corresponding to the triply degenerated Raman active mode, typical of the fluorite-type structure (T_{2g}) [27]. Two other bands with a smaller intensity at ~ 574 cm^{-1} associated to the longitudinal optical (LO) phonon peak and ~ 636 cm^{-1} labeled U3 band are also shown. The LO band is particularly intense due to a resonance effect with the 532 nm wavelength laser. After the S_n irradiations, the T_{2g} band shifts slightly to the lower frequencies. In addition, one band denoted by U1 (~ 532 cm^{-1}) is revealed (Fig. 2.a) and the LO as well as U3 bands intensity increases. These three bands are associated to the formation of atomic-scale defects in the UO_2 crystal and their intensity is linked to the U/O ratio [28-33]. With the S_n ion fluence increase, the T_{2g} band broadens up to 10 cm^{-1} and downshifts (-1 cm^{-1}). This evolution is coupled with the U1, LO and U3 bands intensity increase. The S_e irradiation also induces a modification of the Raman spectra (Fig. 2.b). A T_{2g} band broadening up to 2 cm^{-1} occurs. In addition, the area of LO and U3 bands also increases.

The Raman spectra were fitted with pseudo-Voight functions to compare the local disorder after each irradiation. The evolution of the LO band, associated to the point defect formation, normalized by the T_{2g} band (linked to the fluorite structure), is reported in figure 3.

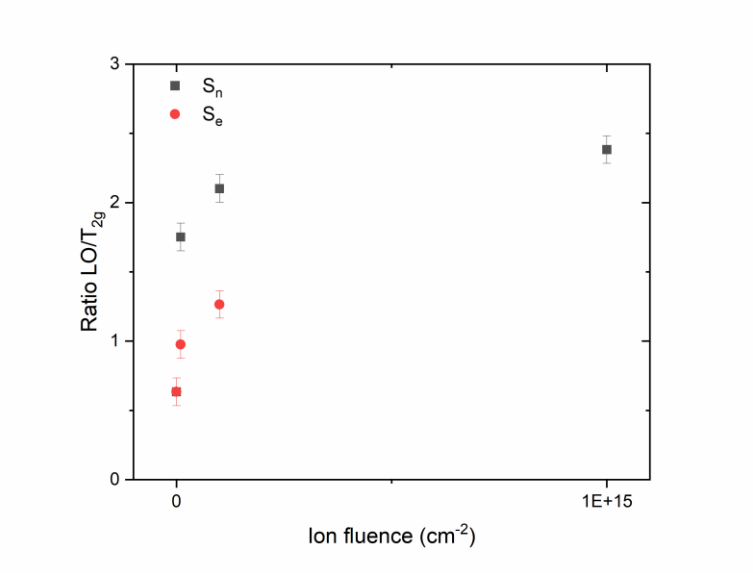

Figure 3: Ratio between the LO and the T_{2g} band areas for the S_n and S_e irradiations as a function of the ion fluence. The considered Raman spectra correspond to the average spectra measured in a Raman map of 30 grains.

For the S_n irradiations, the ratio increases up to 2.4 for the highest fluence highlighting an increase of the local disorder with the S_n fluence increase. After the S_e irradiations, the ratio first increases up to 1 then to 1.2 with the ion fluence. For the two energy-loss regimes, a similar behavior is observed but the ratio is more important for the S_n than for the S_e irradiations.

XRD analysis was also performed. Fig. 4 shows full 2θ-scans recorded on irradiated UO_2 samples with S_n ions (Fig. 4.a), and with S_e ions (Fig. 4.b).

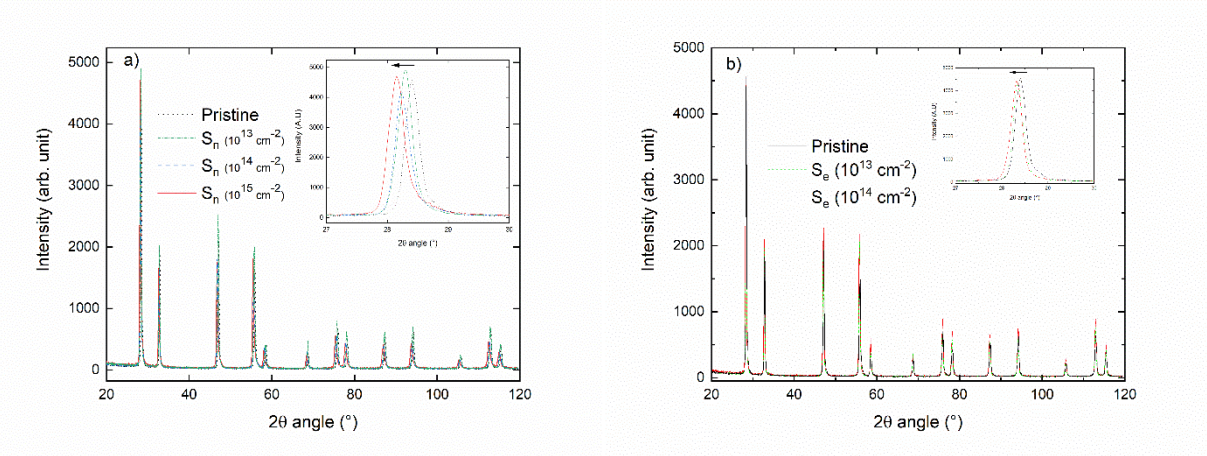

Figure 4: 2θ-scan, recorded at an incidence angle ω = 2°, of UO_2 irradiated with a) 0.9 MeV I ions at fluences of 10^{13}, 10^{14} and 10^{15} cm^{-2} and b) 92 MeV Xe ions at fluences of 10^{13} and 10^{14} cm^{-2}. In insets are shown the 111 diffraction peaks.

For pristine as well as irradiated crystals, all diffraction peaks ascribed to the UO_2 structure are observed, but their relative intensity does not fit with the theoretical one, which is most likely related to texture and grain-size effects despite the use of the spinning mode. If the peak positions are those expected for the pristine crystal, there is a clear peak shift towards lower 2θ angles for irradiated ones. This feature is more easily visible in inset of Fig.4.a that shows a zoom in the 27-30 degrees 2θ-range, where the 111 reflection occurs. It can be seen that the diffraction lines for irradiated crystals are also slightly asymmetric, with a low intensity registered at the peak reference position. This signal originates from the buried un-irradiated region that is little probed. The main peak comes from the damaged layer and this latter exhibits a tensile elastic strain [34, 35]. To evaluate this strain, peak positions are needed, which were determined by fitting the XRD lines, individually, with a Pseudo-Voigt function. We also considered a triaxial stress state, and the Voigt-Reuss-Hill (VRH) approximation [36] to describe UO_2 as a pseudo-elastically isotropic medium. In this framework, the elastic strain is related to $\sin^2\Psi$ according to Equation (1) [26]:

$$\varepsilon = \frac{1+\nu}{E}(1-\sin^2\Psi)\sigma_{//} \qquad (1)$$

In Eq. (1), $\sigma_{//}$ is the in-plane stress experienced by the irradiated layer, and E and ν are the Young modulus and Poisson ratio, respectively. Values of 232 GPa and 0.3 were selected, based on the VHR approximation grounded on elastic properties calculations at the density functional theory level [37]. The plot of the strain as a function of $\sin^2\Psi$ should hence follow a line whose slope is proportional to the stress. The result of this analysis is presented in Fig.4 (see solid lines). For the three irradiation fluences, the strain level is maximum at the lowest Ψ angles, and it decreases to reach zero at Ψ=90 °, *i.e.*, for atomic planes perpendicular to the surface normal. This finding first indicates that the irradiated layers experience a compressive in-plane stress, as the line slopes are negative. Second, the crystalline coherence between the irradiated layer and the unirradiated thick material underneath is maintained, as the in-plane lattice parameter is unchanged (the strain is null); this property was already observed [17, 35]. A maximum strain level of ~0.85 % is measured for the sample irradiated with I ions at 10^{15} cm^{-2} (*i.e.,* a dpa of 7), in agreement with previously reported values [34, 35, 38]; the corresponding in-plane stress reaches ~-1.7 GPa. Expectedly, the strain and stress levels decrease with decreasing the I fluence; the corresponding values are reported in Table 2. Regarding Xe irradiation, the effect is much less than that observed for I irradiation. Indeed, the maximum strain is found to be ~0.2 %, and, given the data point dispersion, discriminating the two ion fluences is hardly possible. Yet, Xe irradiation does lead to the development of a (small) tensile strain (and hence, a low compressive stress); corresponding values are listed in Table 2.

	S_n (10^{15})	**S_n (10^{14})**	**S_n (10^{13})**	**S_e (10^{13})**	**S_e (10^{14})**
ε_{max} (%)	~0.85 ± 0.05 %	~0.6 ± 0.1 %	~0.40 ± 0.05 %	~0.2 ± 0.1 %	~0.2 ± 0.2 %
$\sigma_{//}$(GPa)	~-1.7 ± 0.2	~-1.1 ± 0.2	~-0.8 ± 0.1	~-0.4 ± 0.1	~-0.5 ± 0.1

Table 2: Maximum lattice strain as well as in-plane compressive stress levels experienced by the different UO_2 irradiated crystals.

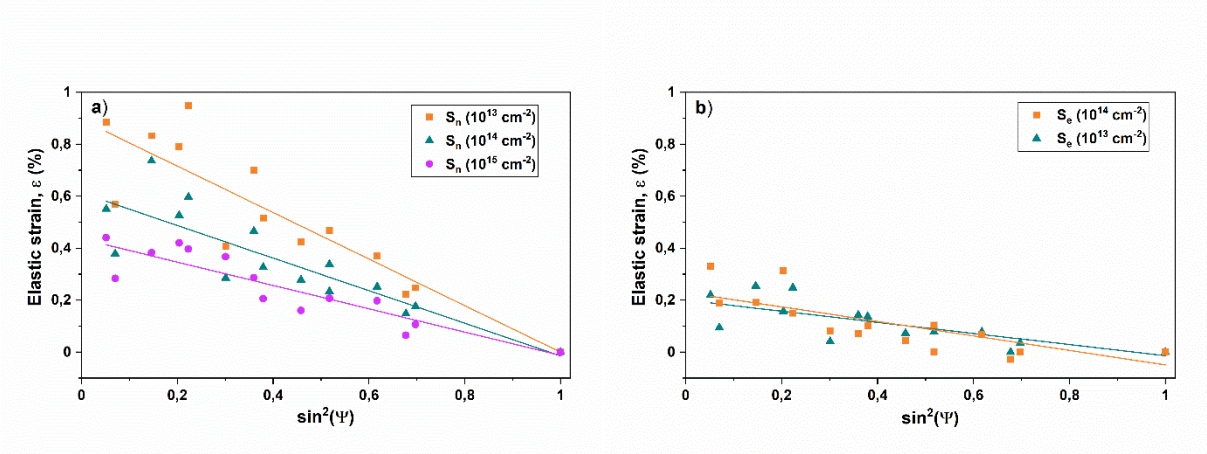

Figure 5: $Sin^2\Psi$ plots of UO_2 samples irradiated with a) 0.9 MeV I ions and; b) 92 MeV Xe ions at the fluences indicated in the legend.

Combined effect of nuclear and electronic energy losses

Raman spectra of a UO_2 pre-irradiated with 0.9 MeV I ions (S_n) at fluences of 10^{14} or 10^{15} cm^{-2} then irradiated with 92 MeV Xe ions (S_e) at an ion fluence of 10^{13} or 10^{14} cm^{-2} were carried out (Fig. 6). The S_e irradiation induces a significant Raman spectra evolution. The T_{2g} band appears less broad (- 6 cm^{-1}). Concerning the defect bands (U1, LO, U3), a qualitative change in the peak shape is observed. Indeed, the LO and U3 band areas are less important. In addition, the U1 band is not observed anymore.

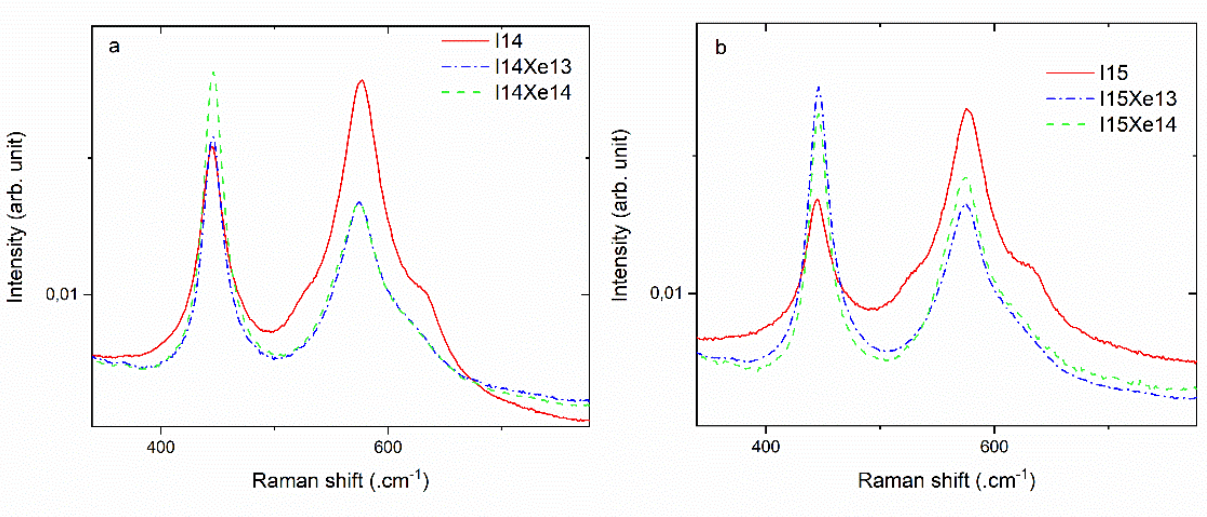

Figure 6: Raman spectra of a UO_2 pre-irradiated with 0.9 MeV I ions (S_n) at fluences of (a) 10^{14} or (b) 10^{15} cm^{-2} then irradiated with 92 MeV Xe (S_e) ions at an ion fluence of 10^{13} or 10^{14} cm^{-2}. The considered Raman spectra correspond to the average spectra measured in a Raman map of 30 grains.

The average Raman spectra were fitted with pseudo-Voight functions. To observe the S_e ion effect on the local disorder for the pre-damaged samples, we show the normalized LO / T_{2g} ratio (divided by the

initial LO / T_{2g} ratio for the pre-damaged sample) as function of the S_e ion fluence. Note that the ratio value for the S_n pre-irradiated sample (S_e fluence equal to 0) is 1.

The subsequent S_e irradiation induces a ratio decrease but with a higher magnitude for the S_n fluence of 10^{15} cm^{-2}. For a higher S_e irradiation fluence, a slight decrease is observed for the S_n fluence of 10^{14} cm^{-2} linked to a small increase of the T_{2G} area (Fig. 6.a). Concerning the pre-damaged sample at a higher S_n fluence, the S_e fluence increase induces a ratio rise mostly due to a slight LO area increase (Fig. 6.b).

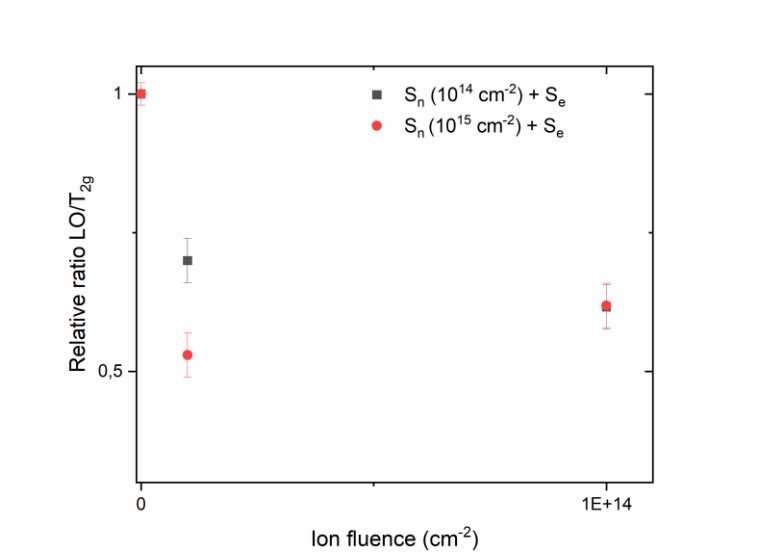

Figure 7: Normalized ratio between the LO and the T_{2g} band areas for the samples irradiated with S_n ion (at 0) and S_n then S_e ion as a function of the high energy ion fluence. The normalized ratio corresponds to the LO/T_{2g} ratio for each condition divided by the corresponding S_n pre-damaged sample. The considered Raman spectra correspond to the average spectra measured in a Raman map of 30 grains.

As explained above, the S_n irradiation leads to the development of a tensile strain localized along the surface normal of the irradiated crystals, associated with a compressive in-plane stress whose magnitude is proportional to the slope of the $\sin^2\Psi$ line plot; this is shown in Fig.8.a for the 10^{15} cm^{-2} S_n fluence. This slope, despite some uncertainty due to the data point dispersion, clearly decreases after the subsequent S_e irradiation at 10^{13} cm^{-2}. It hence comes out that this irradiation leads to a significant decrease in the strain (from maximum ~0.6 % to ~0.2 %) and stress levels; all values are provided in Table 3.

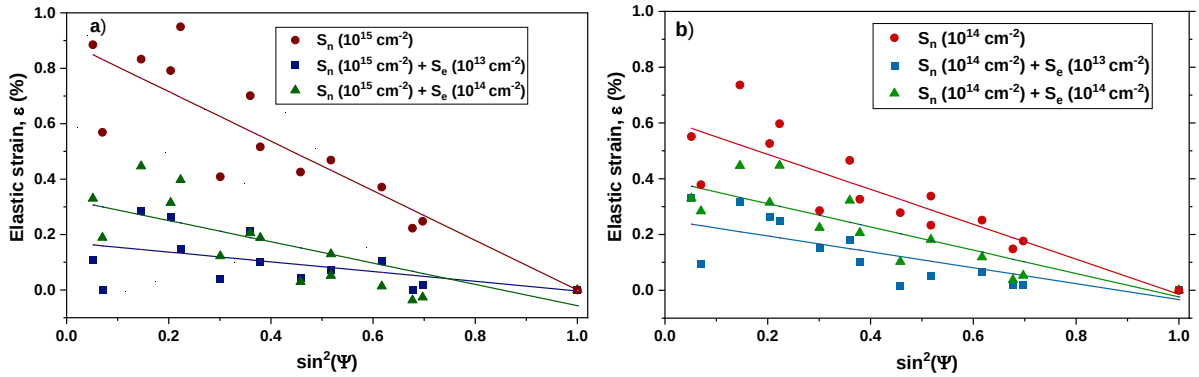

Figure 8: Sin$^2\Psi$ plots of UO_2 samples irradiated with a) 0.9 MeV I ions (S_n) at 10^{15} cm^{-2} and subsequently by Xe ions (S_e) at the indicated fluences; b) same graph as a) but with initial irradiation with I ions at 10^{14} cm^{-2}.

	S_n (10^{15}) + S_e (10^{13})	S_n (10^{15}) + S_e (10^{14})	S_n (10^{14}) + S_e (10^{13})	S_n (10^{14}) + S_e (10^{14})
ε_{max} (%)	~0.2 ± 0.2 %	~0.30 ± 0.05 %	~0.2 ± 0.2 %	~0.40 ± 0.05 %
$\sigma_{//}$(GPa)	~-0.3 ± 0.15	~-0.70± 0.15	~-0.5 ± 0.1	~-0.7 ± 0.1

Table 3: Maximum lattice strain as well as in-plane compressive stress levels experienced by the different UO_2 irradiated crystals.

A similar result, that is, a strain and stress relaxation, was previously observed in dual-beam (S_n concomitant to S_e) irradiation experiments [17]. It is here demonstrated that this phenomenon also takes place for sequential irradiations. Yet, contrary to simultaneous irradiations, the relaxation does not continue when increasing the high-energy ion fluence, since the slope of the sin$^2\Psi$ plots increases after the S_e irradiation at 10^{14} cm^{-2}. This difference might be related to the fact that, as shown in Fig.5, the S_e irradiation induces a slight, but measurable strain level. The very same behavior is observed for the UO_2 crystal irradiated at the 10^{14} cm^{-2} (Fig.8.b). Furthermore, the same strain and stress levels are determined after the S_e irradiation, although the initial one was lower.

DISCUSSION

Respective effects of nuclear and electronic energy losses

In the nuclear energy-loss regime, both the local disorder (evaluated by Raman) and the stress level (determined by XRD) increase with the ion fluence. The corresponding microstructural modification is due to defect formation, in good agreement with previous results [16, 17, 39]. More precisely, for this fluence range (10^{14} and 10^{15} cm^{-2}), dislocation loops are formed [15, 16]. At the highest fluence, the dislocation density and/or dislocation size are larger. As the stress is still increasing from 10^{14} to 10^{15} cm^{-2}, it is likely that only few dislocation lines are present. Indeed, the transformation from dislocation loops to dislocation lines is correlated with a strain and stress relaxation [38, 40, 41], which is not observed here.

The sole S_e irradiation induces a local disorder coupled with a slight stress increase. The contribution of the nuclear energy deposition is very low on the first micrometres for the S_e ion: less than 0.05 dpa is generated by the 92 MeV Xe ions at 10^{15} cm^{-2} (Fig. 1.a). For low-energy ions, in ballistic regime, only a small increase of the local disorder and the stress state was revealed for this damage level [39, 42]. Thus, the observed evolutions after the S_e irradiation can likely be ascribed to the contribution of the electronic energy deposition. The inelastic thermal spike (iTS) model was applied to estimate the deposited energy after the passage of the S_e ions [43, 44]. The calculation details and used parameters can be found in [18]. The energy deposited by the 92 MeV Xe ions on the matrix atoms is shown in figure 9 for different distances from the projectile trajectory (radius).

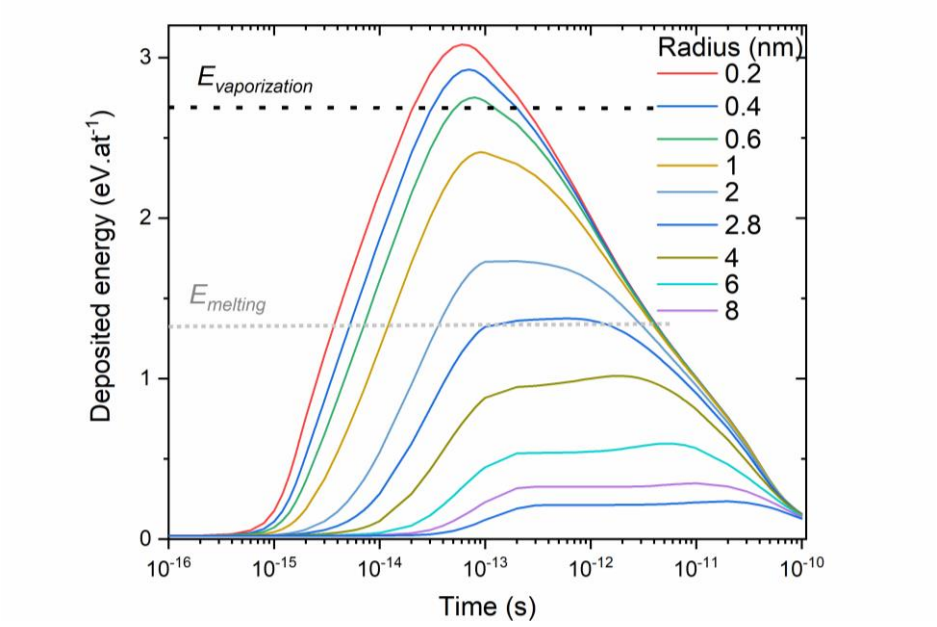

Figure 9: Deposited energy as a function of time for 92 MeV Xe ions in a UO_2 target.

A maximum energy of 2.7 eV.atom^{-1} within a radius cylinder r = 0.4 nm is reached during about 0.2 ps (two atomic vibrations). This energy surpasses the energy needed to reach the vaporization of UO_2 [45]. Thus, the appropriate conditions for forming tracks in UO_2 in terms of energy are fulfilled. The deposited energy on the atoms could then be high enough to induce the formation of latent tracks. The accumulation of ion tracks can lead to the formation of open pores at the surface for a similar electronic energy loss, as shown in [46]. However, we did not observe a surface morphology change after the S_e irradiations (see supplementary materials); this discrepancy can be explained by the lowest ion fluences in the current work as compared to the one used in Ref. [46], and hence, not enough ion tracks are formed to be observed at the surface. Ion track formation in UO_2 induces structural distortions and deformations [5-7] in agreement with our results. CeO_2 and ZrO_2 share the same crystallographic structure and many physical properties than UO_2, and are hence frequently used as surrogates for this compound. In these materials, it was revealed that dislocation loops are also formed around high-energy ion tracks [2, 47]. The lower density inside the tracks is linked to the oxygen atom ejection induced by the S_e ions [47]. The O atoms are then located in an interstitial position and cluster to form dislocation loops [48]. Thus, the current S_e irradiation may probably lead to track formation, which would explain

the Raman and XRD results. Besides, no evolution with the increase of S_e fluence is observed by XRD analysis, and only a small evolution is measured by Raman spectroscopy. The fraction of irradiated surface ($F_{irradiated}$) can be correlated to the ion fluence (ϕ) via a Poisson distribution: $F_{irradiated} = 1- \exp(-\sigma*\phi)$ with σ the surface of the ion impact on the crystal, i.e., πr^2 (Fig. 10). For r = 0.4 nm, the deposited energy is larger than the vaporization energy corresponding to the appropriate conditions for forming tracks. For the low S_e fluence, 4 % is affected by an energy higher than $E_{vaporization}$, and with the fluence increase, the ion track number increases as well, leading to a surface coverage of 39 % for the high S_e fluence. In addition, in the vicinity of the ion track, the deposited energy remains higher than the melting energy (1.31 eV.atom^{-1} [42]) within a radius cylinder of 2.8 nm. For this level of deposited energy, no significant damage creation, such as ion tracks, is observed but in contrast, the induced electronic ionizations can favour defect recombination/clustering processes [41]. As shown in Fig. 10, $E_{melting}$ (r = 2.8 nm) is achieved on 90 % of the surface at 10^{13} cm^{-2}. From 3 x 10^{13} cm^{-2}, this energy level is achieved on the entire surface. Thus, the defect processes are also amplified with the fluence increase. Despite a significant track overlapping, between 10^{13} and 10^{14} cm^{-2}, no significant change in the lattice parameter is observed, which could be due to a partial disorder annealing in the core of the ion tracks; indeed, with swift ions, competing processes of ionizations and displacement events can occur simultaneously [49]. In [6], a clear increase in the lattice parameter was reported in the same fluence range. This discrepancy with our results most likely comes from the difference in the electronic energy-loss level: a higher S_e induces higher radii of ion tracks, as the vaporization energy is reached over a larger area. Thus, the competing process between track formation and defect recombination is probably in favour of the former process with the increase of the electronic energy loss.

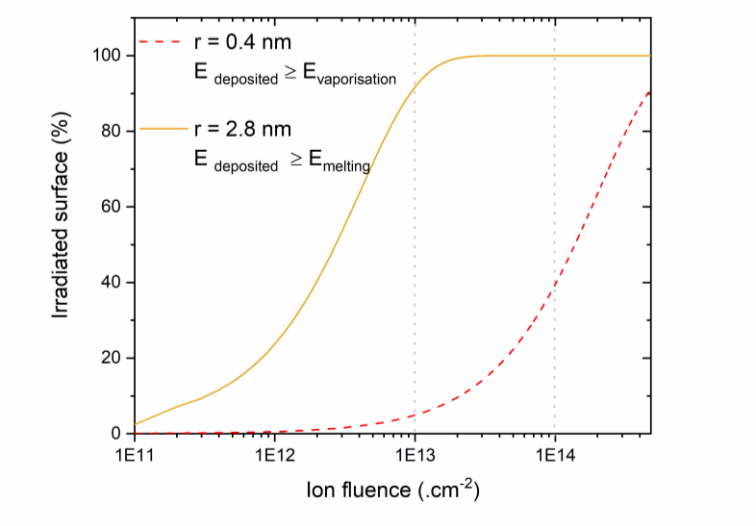

Figure 10: Fraction of irradiated surface by S_e ions (Xe 92 MeV) where the deposited energy is higher than the vaporization energy (r = 0.4 nm) and the melting energy (r = 2.8 nm).

Combined effects of nuclear and electronic energy losses

To investigate the influence of intense electronic energy deposition on the ballistic damage in uranium dioxide, pre-irradiated samples with low-energy ions were subsequently irradiated with high-energy ions (S_n + Se). As clearly demonstrated by the experimental results, the intense electronic ionizations have

an influence on the pre-existing defects. First, for both 10^{14} and 10^{15} cm^{-2} S_n fluences, after a S_e fluence of 10^{13} cm^{-2}, the stress level and the local disorder decrease. As simulated by the iTS calculations, in the vicinity of the ion track, the deposited energy is lower than the vaporization energy but remains important (Fig. 11). Indeed, as above-described, the melting energy (1.31 eV.atom^{-1} [45]) is achieved for a time of 1.8 ps within a radius cylinder of 2.8 nm (see the large, yellow disk in Fig. 11). For other, less energetic conditions, like with 27 MeV Fe ions (with S_e ~ 12 keV/nm), the melting energy is reached in a smaller cylinder of 0.6 nm during a shorter time, 1 ps (as illustrated by the small yellow cylinder Fig. 11). For this level of electronic ionizations, it was shown that the defects created by nuclear energy loss are affected by the ionizations leading to an accelerated defect rearrangement [18].

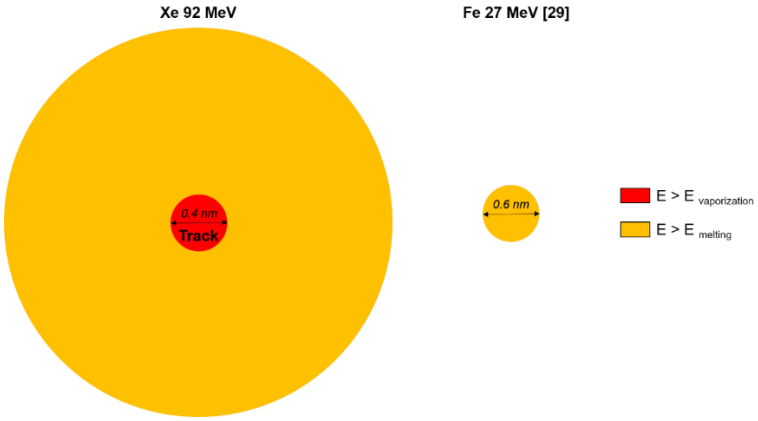

Figure 11: Schematic view of the deposited energy for 92 MeV Xe and 27 MeV Fe ions in a UO_2 target. The red and the yellow colors illustrate the cylinders where the vaporization and the melting energies are deposited.

In the current case of the 92 MeV Xe ion irradiation, for a radius of 2.8 nm, a similar energy is deposited, inducing a significant change in the defect distribution, particularly in the dislocation loop population, as already observed in [18]. Based on our previous works, such a change most likely includes both the development of dislocation lines that explains the stress relaxation, and the recombination/clustering of point defects that leads to a decrease in the LO band intensity. In addition to this latter feature, another, notable change in the Raman spectra is observed after the S_e irradiation: the disappearance of the U1 band. During the sole S_n irradiation, the three U1, LO and U3 bands exhibit a very similar increase in intensity; upon thermal annealing (at 300°C), U1 and U3 bands disappear while the LO band is still observed [33]. During both processes, the three bands have a characteristic behaviour that is not the one here evidenced after the S_e irradiation where a complete disappearance of the sole U1 band is noticed (and LO and U3 bands become less intense). This finding has never been reported so far. It is likely the signature of a reduction in the defect density (decrease of all bands intensity) as well as a change in the defect population (U1 disappearance).

A significant decrease (after the S_e irradiation at 10^{13} cm^{-2}) in the local disorder and in the stress level is hence noticed for both S_n pre-damage ion fluences, but the magnitude of this change, calculated for the stress for instance, is 75 % larger for 10^{15} cm^{-2} than it is for 10^{14} cm^{-2}. As the effect of ionizations on the

ballistic disorder is to accelerate the defect transformation sequence from point defects to dislocation lines through dislocation loops, it is expected that this sequence is more advanced at the highest S_n fluence, and therefore, the stress relaxation related to the development of dislocation lines is more pronounced at this fluence.

With the increase of the S_e fluence, the stress starts to notably redevelop, while the Raman signal only slightly evolves (a small LO intensity increase at 10^{15} cm^{-2}). This difference may be, as explained in section II, due to the different thicknesses probed by the two techniques: XRD is limited to the S_n ion range, while Raman probes deeper than the S_n-affected region. But more important is the fact that the stress increases after the S_e fluence of 10^{14} cm^{-2}. Indeed, for the sole S_e irradiation, almost no change was observed between the two fluences (10^{13} and 10^{14} cm^{-2}). Our results therefore strongly suggest a synergetic effect between pre-existing defects and subsequent inelastic energy loss. The pre-existing defects may have an influence on the material response during the thermal spike process. Such a synergistic effect was observed on pre-damaged $SrTiO_3$ samples where the threshold for the track formation is lowered due to a decrease of the electronic and atomic thermal conductivities increasing, thereby diminishing the electron-phonon coupling [50]. The minimum deposited energy required to induce the track formation may then decrease in the pre-damaged samples. More investigations are required to conclude on this point, but irrefutably, it is shown here that the UO_2 response to electronic energy loss is a complex phenomenon that includes both defect creation and defect annealing, and that depends not only on the level of deposited energy but also on the local defect distribution.

CONCLUSIONS

Pristine and pre-damaged UO_2 pellets were irradiated in the electronic energy loss regime using 92 MeV Xe ions for which S_e~23 $keV.nm^{-1}$ in the surface region. Irradiation of pristine samples induce a local disorder coupled with a slight strain and stress level. As the deposited energy surpasses the energy needed to reach the UO_2 vaporization, this damage is likely due to track formation. In pre-damaged UO_2 samples, the intense ionization events, in addition to inducing a slight disorder, also modify the pre-existing defect distribution. Indeed, after a low S_e irradiation fluence, this change is manifested by a significant stress relaxation and by a local disorder decrease. The former observation is related to the formation of dislocation lines promoted by the electronic energy deposition while the latter finding comes from a decrease in the point defect density (either by recombination or by clustering). At higher Xe fluence, the change in the defect distribution is almost finished, and only the track-induced disorder is observed, as revealed for instance by the stress re-development. The magnitude and the ratio of both processes (i.e., change in defect distribution and track-induced disorder) are shown to depend on the initial microstructure that most likely affects both the way the electronic energy is transferred to the atomic network, and the probability of an interaction between this energy and a pre-existing defect. In summary, intricate synergistic effects take place when both nuclear and electronic energy losses are involved.

Acknowledgments

The irradiation experiments were performed at the Grand Accélérateur National d'Ions Lourds (GANIL) Caen, France, and supported by the French Network EMIR&A. Thanks are given to the CIMAP-CIRIL staff and the GANIL technical staff, especially, C. Grygiel for the technical support during the experiments.

REFERENCES

[1] K. Ohhara, N. Ishikawa, S. Sakai, Y. Matsumoto, O. Michikami, Y. Ohta, Oxygen defects created in CeO2 irradiated with 200MeV Au ions, Nuclear Instruments and Methods in Physics Research Section B: Beam Interactions with Materials and Atoms 267(6) (2009) 973-975.
[2] S. Moll, L. Thomé, L. Vincent, F. Garrido, G. Sattonnay, T. Thomé, J. Jagielski, J.M. Costantini, Damage induced by electronic excitation in ion-irradiated yttria-stabilized zirconia, Journal of Applied Physics 105(2) (2009) 023512.
[3] N. Ishikawa, T. Sonoda, T. Sawabe, H. Sugai, M. Sataka, Electronic stopping power dependence of ion-track size in UO2 irradiated with heavy ions in the energy range of ∼1MeV/u, Nuclear Instruments and Methods in Physics Research Section B: Beam Interactions with Materials and Atoms 314 (2013) 180-184.
[4] T. Wiss, H. Matzke, C. Trautmann, M. Toulemonde, S. Klaumünzer, Radiation damage in UO2 by swift heavy ions, Nuclear Instruments and Methods in Physics Research Section B: Beam Interactions with Materials and Atoms 122(3) (1997) 583-588.
[5] W.F. Cureton, R.I. Palomares, J. Walters, C.L. Tracy, C.-H. Chen, R.C. Ewing, G. Baldinozzi, J. Lian, C. Trautmann, M. Lang, Grain size effects on irradiated CeO2, ThO2, and UO2, Acta Materialia 160 (2018) 47-56.
[6] N. Ishikawa, T. Sonoda, Y. Okamoto, T. Sawabe, K. Takegahara, S. Kosugi, A. Iwase, X-ray study of radiation damage in UO2 irradiated with high-energy heavy ions, Journal of Nuclear Materials 419(1) (2011) 392-396.
[7] K. Hayashi, H. Kikuchi, K. Fukuda, Radiation damage of UO2 by high-energy heavy ions, Journal of Nuclear Materials 248 (1997) 191-195.
[8] F. Garrido, C. Choffel, J.C. Dran, L. Thome, L. Nowicki, A. Turos, Structural modifications in uranium dioxide irradiated with swift heavy ions, Nuclear Instruments and Methods in Physics Research Section B: Beam Interactions with Materials and Atoms 127-128 (1997) 634-638.
[9] C. Onofri, C. Sabathier, C. Baumier, C. Bachelet, H. Palancher, B. Warot-Fonrose, M. Legros, Influence of exogenous xenon atoms on the evolution kinetics of extended defects in polycrystalline UO2 using in situ TEM, Journal of Nuclear Materials 512 (2018) 297-306.
[10] L.-F. He, M. Gupta, C.A. Yablinsky, J. Gan, M.A. Kirk, X.-M. Bai, J. Pakarinen, T.R. Allen, In situ TEM observation of dislocation evolution in Kr-irradiated UO2 single crystal, Journal of Nuclear Materials 443(1) (2013) 71-77.
[11] L.F. He, J. Pakarinen, M.A. Kirk, J. Gan, A.T. Nelson, X.M. Bai, A. El-Azab, T.R. Allen, Microstructure evolution in Xe-irradiated UO2 at room temperature, Nuclear Instruments and Methods in Physics Research Section B: Beam Interactions with Materials and Atoms 330 (2014) 55-60.
[12] C. Onofri, C. Sabathier, C. Baumier, C. Bachelet, H. Palancher, M. Legros, Evolution of extended defects in polycrystalline Au-irradiated UO2 using in situ TEM: Temperature and fluence effects, Journal of Nuclear Materials 482 (2016) 105-113.
[13] C. Onofri, C. Sabathier, G. Carlot, D. Drouan, C. Bachelet, C. Baumier, M. Gérardin, M. Bricout, Changes in voids induced by ion irradiations in UO2: In situ TEM studies, Nuclear Instruments and Methods in Physics Research Section B: Beam Interactions with Materials and Atoms 463 (2020) 76-85.
[14] L.F. He, B. Valderrama, A.R. Hassan, J. Yu, M. Gupta, J. Pakarinen, H.B. Henderson, J. Gan, M.A. Kirk, A.T. Nelson, M.V. Manuel, A. El-Azab, T.R. Allen, Bubble formation and Kr distribution in Kr-irradiated UO2, Journal of Nuclear Materials 456 (2015) 125-132.
[15] M. Bricout, G. Gutierrez, C. Baumier, C. Bachelet, D. Drouan, F. Garrido, C. Onofri, Synergy of electronic and nuclear energy depositions on the kinetics of extended defects formation in UO2, based on in situ TEM observations of ion-irradiation-induced microstructure evolution, Journal of Nuclear Materials 554 (2021) 153088.
[16] M. Bricout, C. Onofri, A. Debelle, Y. Pipon, R.C. Belin, F. Garrido, F. Leprêtre, G. Gutierrez, Radiation damage in uranium dioxide: Coupled effect between electronic and nuclear energy losses, Journal of Nuclear Materials 531 (2020) 151967.

[17] G. Gutierrez, D. Gosset, M. Bricout, C. Onofri, A. Debelle, Effect of coupled electronic and nuclear energy deposition on strain and stress levels in UO2, Journal of Nuclear Materials 519 (2019) 52-56.
[18] G. Gutierrez, M. Bricout, F. Garrido, A. Debelle, L. Roux, C. Onofri, Irradiation-induced microstructural transformations in UO2 accelerated upon electronic energy deposition, Journal of the European Ceramic Society 42(14) (2022) 6633-6641.
[19] L. Lynds, W.A. Young, J.S. Mohl, G.G. Libowitz, X-Ray and Density Study of Nonstoichiometry in Uranium Oxides, Nonstoichiometric Compounds, AMERICAN CHEMICAL SOCIETY1963, pp. 58-65.
[20] G. Leinders, T. Cardinaels, K. Binnemans, M. Verwerft, Accurate lattice parameter measurements of stoichiometric uranium dioxide, Journal of Nuclear Materials 459 (2015) 135-142.
[21] S. Pellegrino, P. Trocellier, S. Miro, Y. Serruys, É. Bordas, H. Martin, N. Chaâbane, S. Vaubaillon, J.P. Gallien, L. Beck, The JANNUS Saclay facility: A new platform for materials irradiation, implantation and ion beam analysis, Nuclear Instruments and Methods in Physics Research Section B: Beam Interactions with Materials and Atoms 273 (2012) 213-217.
[22] J.-P. Crocombette, C. Van Wambeke, Quick calculation of damage for ion irradiation: implementation in Iradina and comparisons to SRIM, EPJ Nuclear Sciences Technologies 5 (2019) 7.
[23] D. Simeone, G. Baldinozzi, D. Gosset, S. Le Caer, J.F. Bérar, Grazing incidence X-ray diffraction for the study of polycrystalline layers, Thin Solid Films, 2013, pp. 9-13.
[24] I.C. Noyan, J.B. Cohen, Residual stress: measurement by diffraction and interpretation, Springer2013.
[25] V. Hauk, Structural and residual stress analysis by nondestructive methods: Evaluation-Application-Assessment, (1997).
[26] U. Welzel, J. Ligot, P. Lamparter, A.C. Vermeulen, E.J. Mittemeijer, Stress analysis of polycrystalline thin films and surface regions by X-ray diffraction, Journal of Applied Crystallography 38(1) (2005) 1-29.
[27] V.G. Keramidas, W.B. White, Raman spectra of oxides with the fluorite structure, The Journal of Chemical Physics 59(3) (1973) 1561-1562.
[28] T. Livneh, Coupling of multi-LO phonons to crystal-field excitations in UO2studied by Raman spectroscopy, Journal of Physics: Condensed Matter 20(8) (2008) 085202.
[29] H. He, D. Shoesmith, Raman spectroscopic studies of defect structures and phase transition in hyper-stoichiometric UO2+x, Physical Chemistry Chemical Physics 12(28) (2010) 8109-8118.
[30] L. Desgranges, G. Guimbretière, P. Simon, C. Jegou, R. Caraballo, A possible new mechanism for defect formation in irradiated UO2, Nuclear Instruments and Methods in Physics Research Section B: Beam Interactions with Materials and Atoms 315 (2013) 169-172.
[31] R. Mohun, L. Desgranges, C. Jégou, B. Boizot, O. Cavani, A. Canizarès, F. Duval, C. He, P. Desgardin, M.F. Barthe, P. Simon, Quantification of irradiation-induced defects in UO2 using Raman and positron annihilation spectroscopies, Acta Materialia 164 (2019) 512-519.
[32] S. Karcher, R. Mohun, T. Olds, M. Weber, K. Kriegsman, X. Zhao, X. Guo, C. Corkhill, D. Field, J. McCloy, Benefits of using multiple Raman laser wavelengths for characterizing defects in a UO2 matrix, Journal of Raman Spectroscopy (2022).
[33] L. Desgranges, A. Canizares, P. Simon, Annealing of the Raman defect peaks in He-implanted UO2, Journal of Nuclear Materials 559 (2022) 153405.
[34] A. Richard, E. Castelier, H. Palancher, J.S. Micha, H. Rouquette, A. Ambard, P. Garcia, P. Goudeau, Multi-scale X-ray diffraction study of strains induced by He implantation in UO2 polycrystals, Nuclear Instruments and Methods in Physics Research, Section B: Beam Interactions with Materials and Atoms 326 (2014) 251-255.
[35] T.H. Nguyen, A. Debelle, A. Boulle, F. Garrido, L. Thomé, V. Demange, Mechanical response of UO2 single crystals submitted to low-energy ion irradiation, Journal of Nuclear Materials 467 (2015) 505-511.
[36] R.J.P.o.t.P.S.S.A. Hill, The elastic behaviour of a crystalline aggregate, 65(5) (1952) 349.

[37] R. Gaillac, P. Pullumbi, F.-X.J.J.o.P.C.M. Coudert, ELATE: an open-source online application for analysis and visualization of elastic tensors, 28(27) (2016) 275201.
[38] A. Debelle, J.-P. Crocombette, A. Boulle, A. Chartier, T. Jourdan, S.R.M. Pellegrino, D. Bachiller-Perea, D. Carpentier, J. Channagiri, T.H. Nguyen, F. Garrido, L. Thomé, Lattice strain in irradiated materials unveils a prevalent defect evolution mechanism, Physical Review Materials 2(1) (2018) 013604.
[39] G. Gutierrez, C. Onofri, S. Miro, M. Bricout, F. Leprêtre, Effect of ballistic damage in UO2 samples under ion beam irradiations studied by in situ Raman spectroscopy, Nuclear Instruments and Methods in Physics Research Section B: Beam Interactions with Materials and Atoms 434 (2018) 45-50.
[40] A. Debelle, J.-P. Crocombette, A. Boulle, E. Martinez, B.P. Uberuaga, D. Bachiller-Perea, Y. Haddad, F. Garrido, L. Thomé, M. Béhar, How relative defect migration energies drive contrasting temperature-dependent microstructural evolution in irradiated ceramics, Physical Review Materials 2(8) (2018) 083605.
[41] X. Jin, A. Boulle, A. Chartier, J.-P. Crocombette, A. Debelle, Analysis of strain and disordering kinetics based on combined RBS-channeling and X-ray diffraction atomic-scale modelling, Acta Materialia 201 (2020) 63-71.
[42] A. Debelle, A. Boulle, F. Garrido, L. Thomé, Strain and stress build-up in He-implanted UO2 single crystals: an X-ray diffraction study, J. Mater. Sci. 46(13) (2011) 4683-4689.
[43] M. Toulemonde, W.J. Weber, G. Li, V. Shutthanandan, P. Kluth, T. Yang, Y. Wang, Y. Zhang, Synergy of nuclear and electronic energy losses in ion-irradiation processes: The case of vitreous silicon dioxide, Physical Review B - Condensed Matter and Materials Physics 83(5) (2011).
[44] M. Toulemonde, E. Paumier, C. Dufour, Thermal spike model in the electronic stopping power regime, Radiation Effects and Defects in Solids 126(1-4) (1993) 201-206.
[45] M. Toulemonde, A. Benyagoub, C. Trautmann, N. Khalfaoui, M. Boccanfuso, C. Dufour, F. Gourbilleau, J.J. Grob, J.P. Stoquert, J.M. Costantini, F. Haas, E. Jacquet, K.O. Voss, A. Meftah, Dense and nanometric electronic excitations induced by swift heavy ions in an ionic CaF2 crystal: Evidence for two thresholds of damage creation, Physical Review B 85(5) (2012) 054112.
[46] T. Sonoda, M. Kinoshita, N. Ishikawa, M. Sataka, A. Iwase, K. Yasunaga, Clarification of high density electronic excitation effects on the microstructural evolution in UO2, Nuclear Instruments and Methods in Physics Research Section B: Beam Interactions with Materials and Atoms 268(19) (2010) 3277-3281.
[47] K. Yasuda, M. Etoh, K. Sawada, T. Yamamoto, K. Yasunaga, S. Matsumura, N. Ishikawa, Defect formation and accumulation in CeO2 irradiated with swift heavy ions, Nuclear Instruments and Methods in Physics Research Section B: Beam Interactions with Materials and Atoms 314 (2013) 185-190.
[48] S. Takaki, K. Yasuda, T. Yamamoto, S. Matsumura, N. Ishikawa, Structure of ion tracks in ceria irradiated with high energy xenon ions, Progress in Nuclear Energy 92 (2016) 306-312.
[49] Y. Zhang, H. Xue, E. Zarkadoula, R. Sachan, C. Ostrouchov, P. Liu, X.-l. Wang, S. Zhang, T.S. Wang, W.J. Weber, Coupled electronic and atomic effects on defect evolution in silicon carbide under ion irradiation, Current Opinion in Solid State and Materials Science 21(6) (2017) 285-298.
[50] W.J. Weber, E. Zarkadoula, O.H. Pakarinen, R. Sachan, M.F. Chisholm, P. Liu, H. Xue, K. Jin, Y. Zhang, Synergy of elastic and inelastic energy loss on ion track formation in SrTiO3, Scientific Reports 5 (2015).

Supplementary material

Defect evolution under intense electronic energy deposition in uranium dioxide

G. Gutierrez[1], H. Guessous[1], D. Gosset[2], M. Bricout[1], I. Monnet[3], F. Garrido[4], C. Onofri[5], G. Adroit[1], A. Debelle[4]

[1] Université Paris-Saclay, CEA, Service de Recherches de Métallurgie Physique, 91191, Gif-sur-Yvette, France.

[2] Université Paris-Saclay, CEA, Service de Recherches de Métallurgie Appliquée, 91191, Gif-sur-Yvette, France.

[3] Centre de recherche sur les ions, les matériaux et la photonique, Normandie Université, ENSICAEN, UNICAEN, CEA, CNRS, CIMAP, 14000 Caen, France.

[4] Laboratoire de Physique des 2 infinis Irène Joliot-Curie (IJCLab), Université Paris-Saclay, Orsay, France.

[5] CEA, DES, IRESNE, DEC, Cadarache, F-13108 St Paul lez Durance, France.

*Corresponding author

E-mail: gaelle.gutierrez@cea.fr

UO_2 surface evolution after high-energy ion irradiations

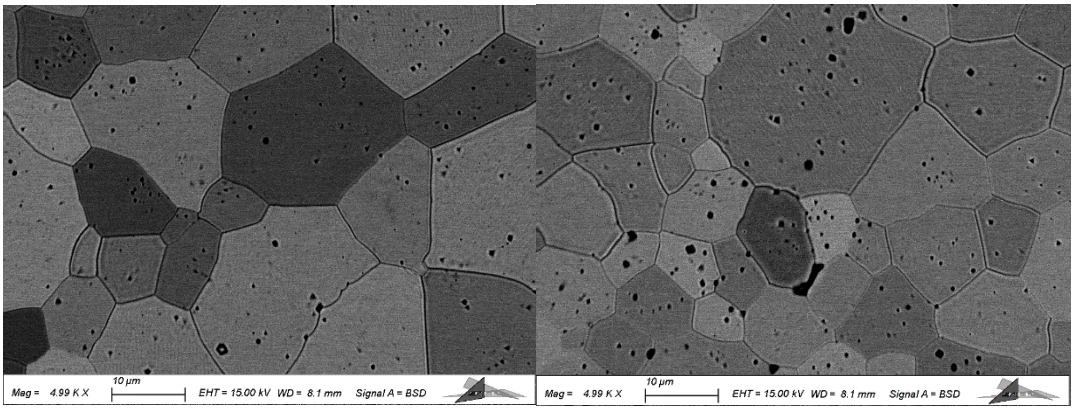

Figure S1: Scanning electron microscopy (SEM) micrographs of a UO_2 sample irradiated with 92 MeV Xe ions at an ion fluence of 10^{14} at.cm^{-2} obtained in backscattered electrons (BSE) mode.